

# Journal of Geophysical Research: Oceans

## RESEARCH ARTICLE

10.1029/2017JC013338

### Key Points:

- Local characteristics of a bottom-trapped coastal front can be confidently extracted from underwater glider observations
- The main driving mechanisms of the Nova Scotia Current can be captured using a two-layer model that includes wind-driven isopycnal tilting
- The conceptual model includes a previously neglected spatial dependency, making it applicable to a wide range of buoyant coastal currents

### Correspondence to:

M. Dever,  
[mdever@whoi.edu](mailto:mdever@whoi.edu)

### Citation:

Dever, M., Skagseth, Ø., Drinkwater, K., & Hebert, D. (2018). Frontal dynamics of a buoyancy-driven coastal current: Quantifying buoyancy, wind, and isopycnal tilting influence on the Nova Scotia Current. *Journal of Geophysical Research: Oceans*, 123, 4988–5003. <https://doi.org/10.1029/2017JC013338>



Received 15 AUG 2017

Accepted 15 MAY 2018

Accepted article online 29 MAY 2018

Published online 28 JUL 2018

## Frontal Dynamics of a Buoyancy-Driven Coastal Current: Quantifying Buoyancy, Wind, and Isopycnal Tilting Influence on the Nova Scotia Current

Mathieu Dever<sup>1</sup> , Øystein Skagseth<sup>2</sup>, Ken Drinkwater<sup>2</sup>, and David Hebert<sup>3</sup> <sup>1</sup>Woods Hole Oceanographic Institution, Falmouth, MA, USA, <sup>2</sup>Institute of Marine Research, Bergen, Norway,<sup>3</sup>Bedford Institute of Oceanography, Dartmouth, Nova Scotia, Canada

**Abstract** The focus of this study is on the relative roles of winds and buoyancy in driving the Nova Scotia Current (NSC) utilizing detailed hydrographic glider transects along the Halifax Line. We define a Hydrographic Wind Index (HWI) using a simplistic two-layer model to represent the NSC and its frontal system. The HWI is based on *local* characteristics of the density front extracted from the glider data (e.g., frontal slope). The impact of wind-driven isopycnal tilting on the frontal slope is estimated and corrected for to accurately scale the buoyancy-driven component of the NSC. Observations from independent current profilers deployed across the NSC confirm that the HWI captures the low-frequency variability of the NSC. The monthly wind-driven flow is estimated to represent between 1.0% ( $\pm 0.1\%$ ) and 48% ( $\pm 1\%$ ) of the total alongshore currents, with a yearly mean of about 36% ( $\pm 1\%$ ). We demonstrate that using local conditions is more appropriate to the study of buoyancy-driven currents ranging over distances on the order of  $\mathcal{O}(100\text{ km})$ , compared to the traditional approach based on *upstream* conditions. Contrary to the traditional approach, the HWI is not affected by the advective time lag associated with the downshelf propagation of the buoyant water coming from the upstream source. However, the HWI approach requires high-resolution data sets, as errors on the estimates of the buoyancy- and wind-driven flows become large as the sampling resolution decreases. Despite being data intensive, we argue that the HWI is also applicable to multisource currents, where upstream conditions are difficult to define.

## 1. Introduction

Buoyancy-driven coastal currents generally exist where a large volume of freshwater is discharged into the ocean (e.g., river estuaries and fjord mouths). The low-density plume grows until it is affected by the Coriolis force (i.e., Rossby radius of deformation) and veers to the right (left) in the Northern (Southern) Hemisphere to propagate *downshelf* (i.e., same direction of propagation as shelf waves). Whether they are generated by one (i.e., single-source currents) or several (i.e., multisource currents) freshwater sources, buoyancy-driven coastal currents constitute a key component of shelf dynamics. Buoyancy-driven currents can have a large impact on the distribution of freshwater, nutrients, sediments, larvae, and pollutants for large distances over a continental shelf (Lentz, 1995; Vikebø et al., 2005). This is partially due to the high coherency in the alongshore direction over distances of the order of  $\mathcal{O}(100\text{--}1,000\text{ km})$ ; Brink, 2016a; Dever et al., 2016). In contrast to the large downshelf impact, the sharp density front associated with buoyancy-driven coastal currents limits cross-shelf exchanges, acting as a barrier between the lower-density plume water and the higher-density ambient shelf water (Brink, 2016b).

Previous studies have shown that both buoyancy and alongshore wind stress, as well as their interaction, must be considered when investigating the driving mechanisms of a coastally trapped current (Csanady, 1982; Münchow & Garvine, 1993a, 1993b; Schwing, 1989, 1992a). Whitney and Garvine (2005, hereafter referred to as WG05) developed an approach that aims at separating and scaling the respective contributions of winds and buoyancy to the Delaware Coastal Current. WG05's approach relies on important assumptions relating the alongshore geostrophic flow of the coastal current to the characteristics of the source of buoyant water (i.e., discharge and density). These *upstream* conditions are generally easier to determine and therefore arguably simplifies the analysis of buoyancy-driven coastal currents such as the Delaware Coastal Current (WG05).

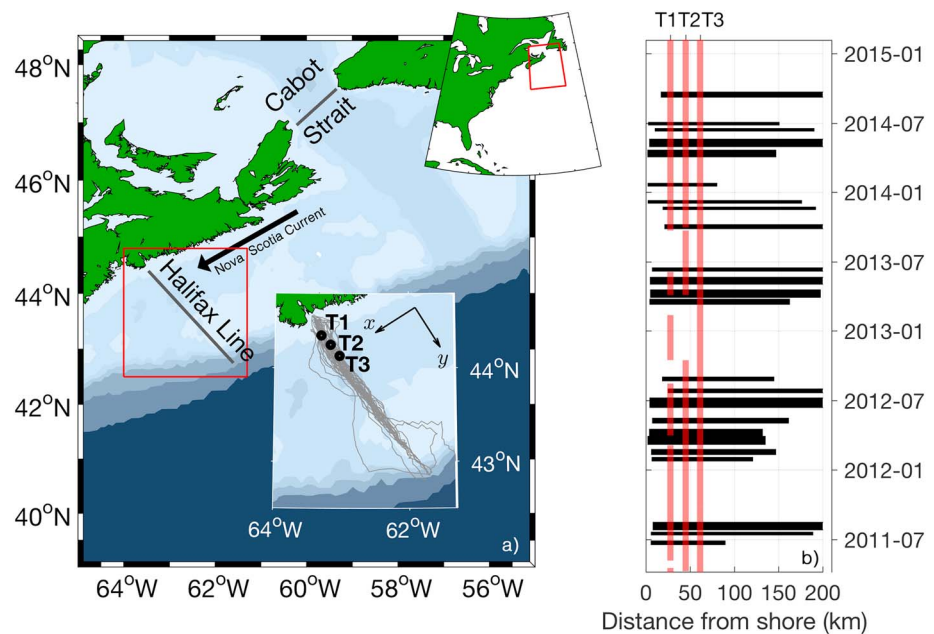


**Figure 1.** (a) Map of the region showing Cabot Strait and the Halifax Line, as well as an arrow indicating the southwestward Nova Scotia Current. Bathymetric contours (blue shading) are shown for the 100-, 200-, 500-, 1 000-, 2,000, and 3,000-m isobaths. The inset (red box) shows the Halifax Line and includes the location of the three ADCPs deployed across the NSC (T1, T2, and T3), the glider tracks (gray lines), and the coordinate system used to define the alongshore and cross-shore components. (b) Data return from the ADCPs (red lines) and the underwater gliders (black lines). ADCP = acoustic Doppler current profiler.

The main goal of this work is to generalize WG05's approach to broaden the applicability of their analysis of the Delaware Coastal Current. To do so, we focus on the Nova Scotia Current (NSC), a southwestward coastal current off the coast of Nova Scotia, and rely on high-resolution transects collected along the Halifax Line (HL) using underwater gliders (Dever et al., 2016; Figure 1). Using a simplistic two-layer model to represent the NSC, we propose to use *local* characteristics of the density front at the HL to estimate the alongshore buoyancy-driven flow (i.e., layer densities and frontal slope). The performance of this approach based on local conditions can be directly assessed using concurrent current measurements collected across the NSC (see Figure 1). Developing an approach based on local conditions introduces a spatial dependency in the analysis, as it no longer relies on the characteristics of the buoyant source. The motivation for this spatially dependent approach is threefold: (1) It allows for the analysis of the spatial variability associated with the key forcing mechanisms, (2) it takes into account the advective time lag associated with the downshelf propagation of the buoyant water coming from the upstream source, making the analysis applicable over distances on the order of  $\mathcal{O}(100\text{ km})$ , and (3) it can be applied to both single-source and multisource coastal currents, for which upstream conditions are difficult to determine.

The data sets used to estimate, validate, and compare our estimates of the buoyancy-driven and wind-driven currents to WG05's method are described in section 2. Section 3 introduces the conceptual model and the approach taken to investigate the roles of buoyancy and surface winds in driving the NSC. The results are presented in section 4. A discussion and concluding remarks are provided in section 5.

## 2. Data Sets

### 2.1. Glider Observations

From June 2011 to September 2014, 62 transects of the Scotian Shelf were completed along the HL using Teledyne Webb Research Slocum gliders (Figure 1). This data set is substantially described in Dever et al. (2016); thus, only a summary of its characteristics is provided here. The glider data have an average resolution of about 0.3 m in the vertical and approximately 850 m in the horizontal, which is much smaller than the typical width of the NSC ( $>40\text{ km}$ ; Dever et al., 2016). Depending on the spatial coverage of the mission, it took from 3 to 11 days for a glider to complete a survey of the HL. Pressure, temperature, and conductivity were measured from 5 m below the surface to 5 m above the bottom or to a maximum depth of 200 m.

Both salinity and potential density were computed using the Gibbs Seawater toolbox in MATLAB. Glider-based observations were gridded following the method outlined in Dever et al. (2016), which is using a block average function with a vertical resolution of 0.5 m and a horizontal resolution of 1 km. Distance from shore was calculated using Devil's Island as a reference point, which is located in the mouth of Halifax Harbor ( $-63.4572^{\circ}\text{W}$ ,  $44.5824^{\circ}\text{N}$ ). Among the 62 transects completed, 19 transects were rejected for this study based on criteria including insufficient cross-shelf coverage, instrument failure, and large differences between the glider track and the HL.

## 2.2. Moored Current Profilers

Velocity measurements were collected using bottom-mounted acoustic Doppler current profilers (ADCPs) along the HL at stations T1 (110-m water depth), T2 (170 m), and T3 (175 m; see inset in Figure 1a). Currents were recorded from April 2008 to April 2015, therefore covering the time period sampled by the underwater gliders. Data gaps in the current velocity time series were caused by either instrument failures or mooring replacements (Figure 1b). The sampling protocol was identical at all three T-stations: every 30 min, the ADCP sent 100 pings with a 3-s delay between each ping. The 100 readings were averaged together to produce a 5-min average of the current speed in the conventional Cartesian coordinate system (east right, north up). Currents were measured at a 4-m vertical resolution, from 10 m off the bottom to minimum 10 m below the surface. A signal frequency of 300 KHz was used at T1, while T2 and T3 required a lower frequency of 150 KHz. Current velocity measurements recorded by bottom-mounted ADCPs were rotated from the eastward and northward directions into the alongshore and cross-shore directions using an angle of  $212^{\circ}$ , measured counterclockwise from east (Dever et al., 2016). This rotation leads to a positive alongshore flow in the *downstream* direction (i.e., same direction of propagation as shelf waves) and to a positive cross-shore flow in the offshore direction (see inset in Figure 1a). To remove the diurnal and semidiurnal tidal signals from the time series, a fifth-order, low-pass, squared Butterworth filter was applied to the velocity records. The cutoff frequency was set to  $8.4 \times 10^{-6}$  Hz (33 hr), at which the power spectral density of the filtered time series is about a third of the initial time series.

## 2.3. Alongshore Winds

The alongshore wind speed is extracted from the European Centre for Medium-Range Weather Forecasts (ECMWF) ERA-interim product that offers a resolution of one eighth of a degree (Dee et al., 2011). Similarly to the current observations, the wind speed is rotated by an angle of  $212^{\circ}$  to obtain the alongshore component and averaged daily over the grid points located within the NSC. A fifth-order, low-pass, squared Butterworth filter with a cutoff period of 72 hr was applied to the time series. ECMWF ERA-Interim alongshore winds are directly compared to wind measurements completed at a buoy located on the inner Scotian Shelf (C44258). The comparison shows that the observed wind variability is reasonably well represented by the ECMWF product ( $r = 0.92$ ,  $p < 0.01$ ), although the alongshore wind speed is slightly overestimated by about 17% of the observed value on average, with a standard deviation of 5%. Due to the frequent data gaps in the observational time series (about 8% of the total time series), the ECMWF ERA-interim data product is used in our study.

## 2.4. Freshwater Discharge

The low-salinity water observed over the inner Scotian Shelf results from the freshwater discharge of the St. Lawrence River (Dever et al., 2016; Smith & Schwing, 1991). This freshwater exits the St. Lawrence Estuary as the Gaspé Current, flows through the Gulf of St. Lawrence along the southern slope of the Laurentian Channel, and exits through Cabot Strait (Urrego-Blanco & Sheng, 2014). Previous estimates of the freshwater outflow at Cabot Strait range from  $1.5$  to  $3.0 \times 10^4$   $\text{m}^3/\text{s}$  (El-Sabh, 1977; Ohashi & Sheng, 2013). The freshwater flux through Cabot Strait is therefore many orders of magnitudes larger than any other Nova Scotian River and indisputably dominates in this region. The southwestward propagation of salinity anomalies through Cabot Strait and along the coast of Nova Scotia was previously observed and is estimated to take about 3 months to reach the HL (Drinkwater et al., 1979). Information on the transport and density of the water discharged from the Gulf of St. Lawrence onto the Scotian Shelf through Cabot Strait (i.e., the upstream conditions; see Figure 1) is limited due to a lack of in situ measurements. To quantify the upstream conditions, this study relies on model outputs generated by a one-way nested ocean circulation model based on the Princeton Ocean Model. The numerical model is described and validated in Shan et al. (2016). The model domain used in our study (submodel L2 in Shan et al., 2016) includes the Gulf of St. Lawrence, Scotian Shelf, and Gulf of Maine, with a horizontal resolution of  $1/16^{\circ}$  and  $40\sigma$  layer in the vertical. Numerical simulations covered the years 2011 and 2012 and included realistic atmospheric forcing taken from the North American Regional Reanalysis.

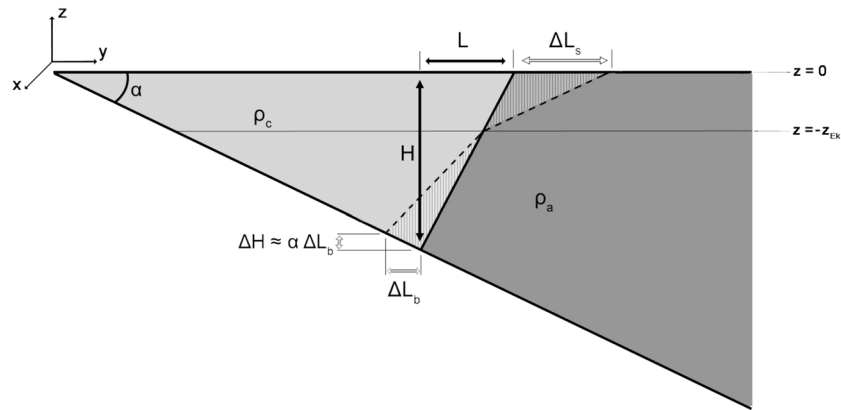


**Figure 2.** Diagram of a buoyancy-driven coastal current. The parameters from equation (2) are indicated on the diagram: the frontal width  $L$ , the frontal depth  $H$ , and the average densities of coastal water  $\rho_c$  and ambient shelf water  $\rho_a$ . The change in frontal width and frontal depth associated with the tilting of the density front under upwelling-favorable winds are also indicated (equations (13)–(15)). The tilting occurs at the Ekman depth ( $z_{Ek}$ ). The bottom horizontal displacement  $\Delta L_b$  is estimated based on the fact that the offshore transport in the upper layer ( $z < -z_{Ek}$ ; hatched regions) must be equal to the onshore transport in the rest of the water column ( $z > -z_{Ek}$ ; hatched regions). The bottom slope  $\alpha$  is also shown.

More information on the model configuration and validation can be found in Shan et al. (2016). The monthly averaged outward transport  $Q_r$  and the averaged density of the outflow  $\rho_r$  at Cabot Strait are computed in the model over 16 grid points.

### 3. Methods: Two-Layer Conceptual Model

A simplistic conceptual model is used in this study to investigate the relative roles of buoyancy and surface winds in driving the NSC. This conceptual model is characterized by a two-layer flow with a quiescent bottom layer (also known as a one-and-a-half layer flow). The upper layer, formed of coastal water of averaged density  $\rho_c$ , is separated from the ambient shelf water of averaged density  $\rho_a$  (with  $\rho_a > \rho_c$ ) by a sharp density front (see Figure 2). The density front is *bottom trapped* and therefore intersects the ocean surface as well as the bottom (as opposed to *surface-trapped* fronts; Chapman & Lentz, 1994; Lentz & Helfrich, 2002). The next few sections detail the approach used to estimate the alongshore wind- and buoyancy-driven flows in this idealized setup.

#### 3.1. Alongshore Buoyancy-Driven Current

Since the width of the NSC is larger than the Rossby radius of deformation (Dever et al., 2016), scaling arguments show that the cross-shelf momentum balance is mostly geostrophic (Garvine, 1995; Smith & Schwing, 1991). Cross-shelf conditions over the Scotian Shelf can be considered as a two-layer system, with the low-density coastal water sitting on top of the higher-density ambient shelf water (Figure 2). Thermal wind dynamics are used to estimate the alongshore buoyancy-driven current (Gill, 1982). Assuming that the lower layer is motionless compared to the upper layer, the alongshore velocity in the upper layer can be obtained using

$$U_{geo} = \frac{g'}{f} \frac{dh_f}{dy}, \quad (1)$$

where  $dh_f/dy$  represents the slope of the interface separating the two layers (i.e., the density front) and  $g'$  is the reduced gravity defined as  $g' = g(\rho_a - \rho_c)/\rho_a$ , where  $\rho_c$  and  $\rho_a$  are the averaged densities of low-density coastal water and ambient shelf water, respectively (Figure 2).

Assuming a wedge-shaped current, the slope of the front is the ratio of the frontal depth ( $H$ ) to the frontal width ( $L$ ; Figure 2)

$$U_{geo} = \frac{g'H}{fL}. \quad (2)$$

Estimating the alongshore geostrophic current therefore relies on four important parameters: the average density of the coastal water  $\rho_c$ , the average density of the ambient shelf water  $\rho_a$ , the frontal depth  $H$ , and the

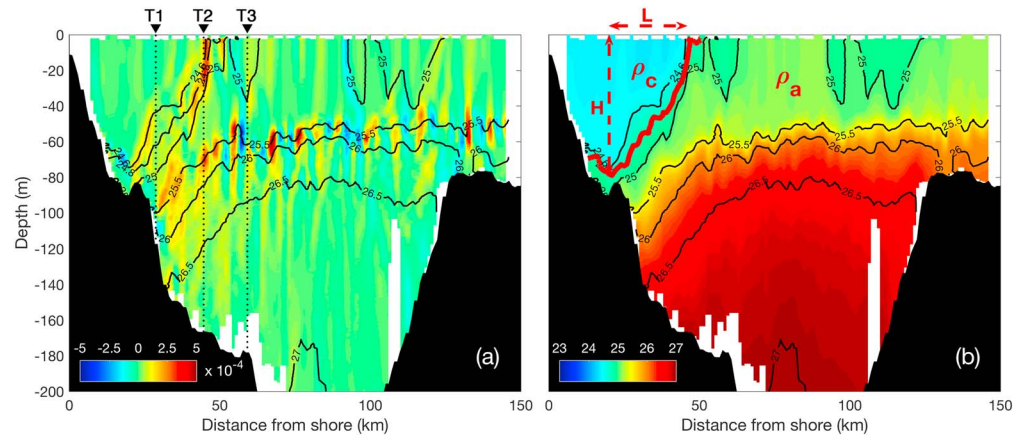


**Figure 3.** Example of the detection of the density front, based on a transect of potential density completed between 9 and 17 February 2012. (a) The computed offshore density gradient (in kilogram per cubic meter per meter), where potential density contours are superimposed (black line) along with the location of stations T1, T2, and T3 (dotted line). (b) The potential density field (in kilogram per cubic meter), with the isopycnal selected by the algorithm to describe the density front (thick red line), as well as the four parameters extracted from the transect ( $L$ ,  $H$ ,  $\rho_c$ , and  $\rho_a$ ).

frontal width  $L$ . To extract these frontal characteristics from a density transect, the density front separating the coastal water from the ambient shelf water must first be defined. A two-step algorithm was thus developed to (1) compute the cross-shore density gradient and (2) select the isopycnal experiencing the largest density gradient in the top 20 m of the water column (see Figure 3). Applying this criterion to the upper water column improves the reliability of the algorithm, since it guarantees that the density front detected by the algorithm intersects the ocean surface. This precaution prevents the algorithm from selecting other subsurface density fronts.

The alongshore geostrophic transport can thus be estimated from the product of the alongshore flow (see equation (2)) and the cross-sectional area of the current:

$$Q_{\text{geo}} = U_{\text{geo}} \frac{HL}{2} = \frac{g'H^2}{2f}. \quad (3)$$

The cross-sectional area of the current is taken as  $HL/2$  based on the assumption that no horizontal density gradient exists inshore of the location where the front intersects the bottom (see Figure 2). In other words, the density variability within a layer is small compared to the density difference between the two layers, constraining the geostrophic flow to triangular region formed by  $H$  and  $L$ .

Both equations (2) and (3) require knowledge about the density field and the frontal geometry, which have proven to be difficult to estimate without the availability of relatively high resolution measurements (e.g., glider data). In their study of the Delaware Current, WG05 get around this issue by substituting the length scale  $L$  in equation (2) by  $KR_b$ , where  $K$  thus represents the ratio of the across-shore length scale of the current  $L$  to the Rossby radius of deformation  $R_b = \sqrt{g'H}/f$  and is sometimes referred to as the Kelvin number (Garvine, 1995). The Kelvin number is scaled for the NSC based on a current's width of about 35 km and a Rossby radius estimated at about 8 km (Drinkwater et al., 1979; Loder et al., 2003), yielding  $K \approx 4$ . Using equation (3) to define  $H$  in equation (2), we obtain

$$U_{\text{geo}} = \frac{1}{K} (2g'Q_{\text{geo}}f)^{1/4}. \quad (4)$$

Estimating  $g'$  and  $Q_{\text{geo}}$  in equation (4) still requires information on the density and velocity fields within the coastal current. WG05 therefore link the geostrophic transport  $Q_{\text{geo}}$  and reduced gravity  $g'$  to the river discharge  $Q_r$  and reduced gravity of the river  $g'_r$  by assuming that the mixing between river water and ambient shelf water is the only process taking place. Using  $g'Q_{\text{geo}} = g'_rQ_r$ , equation (4) becomes

$$U_{\text{dis}} = \frac{1}{K} (2g'_rQ_rf)^{1/4}, \quad (5)$$



where  $U_{\text{dis}}$  is the alongshore geostrophic current calculated from the river discharge  $Q_r$ . The reduced gravity of the river is defined as  $g'_r = g(\rho_a - \rho_r)/\rho_a$ , where  $\rho_r$  is the density of the river water.

In this study, we take advantage of the high spatial resolution of the glider data to directly estimate the alongshore geostrophic flow from local characteristics (equation (2) and Figure 3). This method is directly compared to WG05's approach by computing both  $U_{\text{geo}}$  from equation (2) and  $U_{\text{dis}}$  from equation (5) at the HL. The results of this comparison are presented in section 4 and discussed in section 5.

### 3.2. Alongshore Wind-Driven Flow

The barotropic response in alongshore currents to surface winds can be estimated based on the steady state Ekman theory, where the frictional forces are balanced by the rotational term (Dever, 2017; WG05):

$$-fV_{\text{wind}} = \frac{\tau_{sx} - \tau_{bx}}{\rho_0 H} \quad (x \text{ comp}) \quad (6)$$

$$fU_{\text{wind}} = \frac{\tau_{sy} - \tau_{by}}{\rho_0 H} \quad (y \text{ comp}), \quad (7)$$

where ( $U_{\text{wind}}$ ,  $V_{\text{wind}}$ ) are the alongshore and cross-shore depth-averaged barotropic flow driven by winds, respectively;  $f$  is the Coriolis parameter;  $\tau_s$  is the surface wind stress;  $\tau_b$  is the bottom stress;  $\rho_0$  is a reference density used under the Boussinesq approximation; and  $H$  is the depth of the water column. The analysis of current measurements at the HL showed that the alongshore currents are approximately 2 orders of magnitude larger than the cross-shelf currents (Dever et al., 2016). The left-hand term in equation (7) can thus be assumed to be small, leading to a balance between the alongshore surface wind stress ( $\tau_{sx}$ ) and the alongshore bottom stress ( $\tau_{bx}$ ). This approximation is commonly referred to as the frictionally adjusted flow theory and was first developed in Csanady (1974). In this work, Csanady (1974) defines an adjustment time scale ( $t_f$ ) that estimates the time required for the water column to reach that frictionally adjusted state, which is defined as

$$t_f = \frac{H}{2\sqrt{\frac{\tau_{sx} C_{Da}}{\rho}}}, \quad (8)$$

where  $C_{Da}$  is the depth-averaged equivalent to the traditional bottom drag  $C_D$ , defined by  $C_{Da} = (8 + 1/\sqrt{C_D})^{-2}$  (Csanady, 1982). Previous results obtained from both observational and modeling studies conducted over the Scotian Shelf demonstrated that this assumption is valid for waters as deep as 100 m in this region, for time scales longer than the adjustment time scale (Sandstrom, 1980; Schwing, 1992a, 1992b). Using realistic wind stress observed over the Scotian Shelf, the adjustment time scale is estimated to be less than 3 days on average for the NSC, where the water depth is about 100 m. A squared Butterworth filter with a cutoff period of 72 hr is therefore used to filter out variability at higher frequencies in the wind time series (see section 2). Both surface and bottom stresses are expressed using a quadratic law:

$$\tau_{sx} = \rho_{\text{air}} C_{10} |U_{10}| U_{10} \quad (9)$$

$$\tau_{bx} = \rho_0 C_{Da} |U_{\text{wind}}| U_{\text{wind}}, \quad (10)$$

where  $\rho_{\text{air}}$  is the air density ( $1.2 \text{ kg/m}^3$ ),  $C_{10}$  is the surface drag coefficient ( $1.2 \times 10^{-3}$ ), and  $U_{10}$  is the alongshore wind speed at 10 m above the sea surface,  $\rho_0$  is the reference density ( $1,025 \text{ kg/m}^3$ ), and  $C_{Da}$  is the depth-averaged bottom drag coefficient ( $2.0 \times 10^{-3}$ ). By setting  $\tau_{sx} = \tau_{bx}$ , equations (9) and (10) can be combined to estimate the wind-forced alongshore current:

$$U_{\text{wind}} = \sqrt{\frac{\rho_{\text{air}} C_{10}}{\rho C_{Da}}} U_{10}, \quad (11)$$

$U_{\text{wind}}$  is therefore directly proportional to the alongshore wind speed, with a factor of about 0.02. This result is in agreement with the analysis presented in Sandstrom (1980), where the maximum expected alongshore currents generated by surface winds scale to approximately 3% of the alongshore wind speed over the inner Scotian Shelf.

### 3.3. Wind-Driven Isopycnal Tilting

Alongshore winds generate a cross-shore Ekman transport, resulting in isopycnal tilting (Figure 2); an upwelling (downwelling) favorable wind stress will increase (decrease) the width of the current by advecting the density front offshore (onshore) in the upper layer. At the bottom, the density front will shoal (deepen) due to the pumping (sinking) of water along the bottom slope. Because the geometry of the front directly—and only—affects the estimate of  $U_{\text{geo}}$  through equation (2), part of  $U_{\text{geo}}$  is due to the interaction of the density front with the surface winds. Neglecting wind-driven isopycnal tilting would therefore bias our estimates toward the buoyancy-driven component and underestimate the role of local winds. It is important to stress the distinction between the isopycnal tilting due to the equilibrium in  $U_{\text{geo}}$  described in equation (2) and the wind-driven isopycnal tilting that is generated by alongshore winds. Correcting for the latter provides insights on what the geostrophic current would be if there was no wind.

Here the impact of alongshore winds on the frontal slope is accounted for by considering the change in the geometry of the front generated by surface winds using a simplistic conceptual model ( $\Delta H$ ,  $\Delta L_s$ , and  $\Delta L_b$  in Figure 2). The frontal displacement associated with the alongshore surface winds is balanced by the time-integrated cross-shore Ekman transport  $\tau_{sx} / \rho f z_{\text{Ek}}$  and can be estimated if both the original geometry of the front and the surface wind stress are known. Assuming that isopycnals tilt at the Ekman depth  $z_{\text{Ek}}$ , the change in the current width at the surface ( $\Delta L_s$ ) can be calculated using

$$\Delta L_s = - \int \frac{2\tau_{sx}}{\rho f z_{\text{Ek}}} dt, \quad (12)$$

where the frontal displacement at the surface (term on the left-hand side) is balanced by the time-integrated, depth-averaged, cross-shelf Ekman transport  $\tau_{sx} / \rho f z_{\text{Ek}}$  (term on the right-hand side). The factor 2 arises from the assumption of a linear velocity profile throughout the Ekman layer, with a maximum flow at the surface and no flow at the Ekman depth. Equation (12) is similar to the excursion length previously defined in Fong et al. (1997). Assuming that the integrand is constant over one time step  $\Delta t$ , equation (12) can be discretized:

$$\Delta L_s = - \sum_i \frac{2\tau_{sx_i}}{\rho f z_{\text{Ek}}} \Delta t, \quad (13)$$

where  $i$  is the number of time steps and  $\tau_{sx_i}$  is the alongshore wind stress averaged over  $\Delta t$  at time step  $i$ . The time scale  $\Delta t$  corresponds to the frictional adjustment time mentioned in section 3.2. For mass conservation, the cross-shore Ekman transport in the surface Ekman layer ( $z > -z_{\text{Ek}}$ ) is compensated by an equal transport in the opposite direction over the lower part of the water column ( $z < -z_{\text{Ek}}$ ). The horizontal displacement of the front at the bottom ( $\Delta L_b$ ) can thus be computed using

$$\Delta L_b = - \sum_i \frac{2\tau_{sx_i}}{\rho f (H_{i-1} - z_{\text{Ek}})} \Delta t, \quad (14)$$

where  $H_{i-1}$  is the frontal depth at the previous time step. The change in the frontal depth can then be deduced by scaling  $\Delta L_b$  with the bottom slope  $\alpha$  (Figure 2):

$$\Delta H = -\Delta L_b \tan(\alpha) \sim -\alpha \Delta L_b, \quad \text{for } \alpha \ll 1. \quad (15)$$

In this study, the bottom slope over the inner Scotian Shelf is estimated from topographic data and is set to  $\alpha = 0.03$ . The Ekman depth ( $z_{\text{Ek}}$ ) is chosen to be either 25 m or half of the frontal depth, whichever is the shallowest. This depth corresponds to the average Ekman depth scaled using the vertical eddy viscosity parameter used in the submodel L2 presented in section 2.4 ( $\sim 3 \times 10^{-3} \text{ m}^2/\text{s}$ ; Shan et al., 2016). We identify two limiting cases for the change in frontal width due to isopycnal tilting. The first one prevents the density front from spreading farther than 170 km from shore, which corresponds to the width of the Scotian Shelf at the HL. This is based on the maximum frontal width measured over the observation period and is justified by the fact that other mechanisms come into play when approaching the shelf break, preventing further widening of the coastal front (e.g., shelf break jet and front; Pickart et al., 1999). The second limiting case is to prevent an *inshore* tilting of the front, which is when the density front has a negative slope. Sustained downwelling winds could theoretically generate a negatively sloped density front, which would lead to convective mixing,

homogenizing the water column. Once the wind-driven isopycnal tilting is determined, the observed current geometry at any given time can be corrected to exclude the wind-driven component:

$$U_{\text{geo}}^c = \frac{g'H^c}{fL^c}, \text{ where } \begin{cases} H^c = H - \Delta H \\ L^c = L - (\Delta L_s + \Delta L_b), \end{cases} \quad (16)$$

where the superscript  $c$  denotes the corrected estimates. While  $U_{\text{geo}}$  provides an estimation of the buoyancy-driven flow,  $U_{\text{geo}}^c$  estimates the magnitude of the buoyancy-driven flow in the absence of winds. The difference between  $U_{\text{geo}}$  and  $U_{\text{geo}}^c$  corresponds to the baroclinic flow resulting from the isopycnal tilting induced by alongshore surface winds. This difference is reattributed to  $U_{\text{wind}}$  to define  $U_{\text{wind}}^c$  using

$$U_{\text{wind}}^c = U_{\text{wind}} + (U_{\text{geo}} - U_{\text{geo}}^c). \quad (17)$$

The first term in equation (17) therefore corresponds to the wind-driven barotropic flow, while the second term results from the change in the alongshore velocity due to the wind-driven isopycnal tilting. While this correction is reattributed to the wind component, it only exists because of the interaction between the density front and the surface winds.

### 3.4. Hydrographic Wind Index

We define a Hydrographic Wind Index (HWI) that represents the ratio of the wind-driven current to the buoyancy-driven flow within the NSC. Both noncorrected and corrected HWIs are computed using

$$HWI = \frac{U_{\text{wind}}}{U_{\text{geo}}} \quad (18)$$

$$HWI^c = \frac{U_{\text{wind}}^c}{U_{\text{geo}}^c}. \quad (19)$$

Comparing HWI and HWI<sup>c</sup> provides valuable information on the role of alongshore winds in modulating the shape of the bottom-trapped density front. Both the sign and the magnitude are important when interpreting HWI (and HWI<sup>c</sup>):

1. If  $HWI > 1$ ,  $U_{\text{wind}}$  dominates and is reinforced by  $U_{\text{geo}}$ , as they both have the same downshelf direction.
2. If  $0 < HWI < 1$ ,  $U_{\text{geo}}$  dominates and is reinforced by  $U_{\text{wind}}$ , as they both have the same downshelf direction.
3. If  $-1 < HWI < 0$ ,  $U_{\text{geo}}$  dominates and is slowed down by  $U_{\text{wind}}$ , as they act in opposite directions.
4. If  $HWI < -1$ ,  $U_{\text{wind}}$  dominates and is slowed down by  $U_{\text{geo}}$ , as they act in opposite directions. This situation leads to a flow reversal, which occurs when the coastal current flows upstream (i.e., opposite direction to shelf wave propagation). Such flow reversals have previously been observed and documented (Münchow & Garvine, 1993a; Sanders & Garvine, 2001).

### 3.5. Method Validation

The performance of the HWI approach can be assessed at the HL by comparing the alongshore currents and transport estimated using equations (2) and (11), with the alongshore currents and transport computed from the ADCPs deployed at the three T-stations (Figure 1). These ADCPs were ideally located to capture the NSC's variability and therefore constitutes an independent data set to directly validate the HWI method (Dever et al., 2016; Figure 3).

The buoyancy-driven flow is scaled using the modal values of each parameter observed at the HL in equation (2). We take  $g = 9.81 \text{ m/s}^2$ ,  $\rho_a = 1,025.4 \text{ kg/m}^3$ ,  $\rho_c = 1,024.5 \text{ kg/m}^3$ ,  $H = 87 \text{ m}$ ,  $L = 50 \text{ km}$ , and  $f = 1.02 \times 10^{-4} \text{ s}^{-1}$ . The buoyancy-driven flow at the HL therefore scales to

$$U_{\text{geo}} = 0.15 \pm 0.01 \text{ m/s},$$

where the positive sign means southwestward and the uncertainty is estimated using the standard deviation of each parameter and the error propagation formula detailed in Appendix A. The alongshore geostrophic transport ( $Q_{\text{geo}}$ ) can be calculated by multiplying the alongshore geostrophic flow by the cross-sectional area  $HL/2$ :

$$Q_{\text{geo}} = 0.32 \pm 0.01 \text{ Sv}.$$



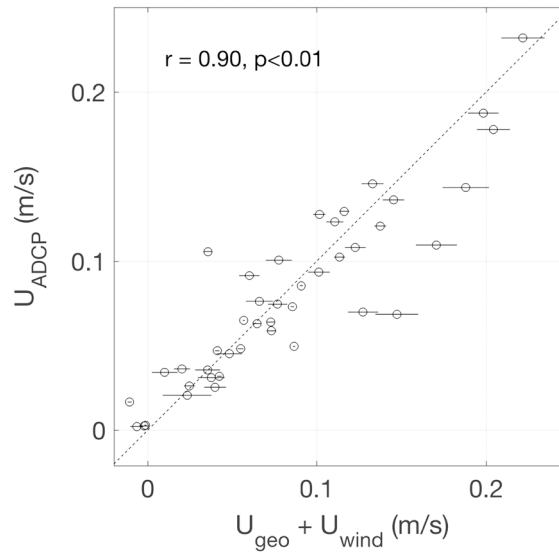


**Figure 4.** Comparison between the alongshore flow computed from ADCP observations ( $U_{\text{ADCP}}$ ) and obtained when adding the buoyancy-driven ( $U_{\text{geo}}$ ; see equation (2)) and wind-driven ( $U_{\text{wind}}$ ; see equation (11)) currents obtained from the conceptual model described in section 3. The dashed line represent the 1:1 line. The correlation coefficient and the associated  $p$  value are indicated. The error associated with each alongshore current estimation from the conceptual model are indicated with error bars (see Appendix A). ADCP = acoustic Doppler current profiler.

The wind-driven flow at the HL is scaled using  $\rho_{\text{air}} = 1.2 \text{ kg/m}^3$ ,  $\rho = 1,025 \text{ kg/m}^3$ ,  $C_{10} = 1.1 \times 10^{-3}$ ,  $C_{Da} = 2 \times 10^{-2}$ , and  $U_{10} = -2.28 \text{ m/s}$  (equation (11)). The wind-driven flow at the HL therefore scales to

$$U_{\text{wind}} = -0.06 \text{ m/s},$$

where the negative sign means northeastward. The corresponding alongshore wind-driven transport is

$$Q_{\text{wind}} = -0.12 \pm 0.01 \text{ Sv}.$$

The total alongshore transport within the NSC ( $Q_{\text{geo}} + Q_{\text{wind}}$ ) is therefore scaled to  $0.20 \pm 0.01 \text{ Sv}$ , which is comparable to the modal value of  $0.23 \text{ Sv}$  obtained based on ADCP current records collected along the HL (see Dever et al., 2016).

The same ADCP current records can also be used to further evaluate the reliability of the HWI method, by directly comparing the time series of the total alongshore flow ( $U_{\text{wind}} + U_{\text{dis}}$ ) estimated using equations (11) and (2), with the average alongshore flow measured by the three ADCPs during each glider deployment (Figure 4). The two estimates present a high correlation coefficient ( $r=0.90$ ,  $p < 0.01$ ), with a root-mean-square value of about  $0.03 \text{ m/s}$ . It is important to note that correcting for the wind-driven isopycnal tilting will not affect this result as it only redistributes a portion of  $U_{\text{geo}}$  to  $U_{\text{wind}}$ , leaving the sum unchanged.

## 4. Results

### 4.1. Frontal Characteristics and Buoyancy-Driven Flow

The baroclinic component of the NSC is predominantly southwestward with speeds ranging between  $0.07 \text{ m/s}$  in summertime and  $0.20 \text{ m/s}$  during the winter (Figure 5d). This result agrees with the current speeds reported in the literature (Dever et al., 2016; Drinkwater et al., 1979; Smith & Schwing, 1991; Urrego-Blanco & Sheng, 2014). It is interesting to note that this noncorrected  $U_{\text{geo}}$  follows the seasonal cycle of the frontal slope ( $H/L$ ; Figure 5d) but is not in phase with the seasonal cycle of the density gradient (Figure 5c). Despite the reduced gravity reaching its maximum in the summer and fall, when the density difference between buoyant coastal water and ambient shelf water is the largest, the buoyancy-driven flow in summer and fall is the weakest. This can be explained by the wide and shallow (i.e., flat) density front observed in this season, representing a stratified water column. By comparison, the density front is the narrowest and deepest (i.e., steepest)

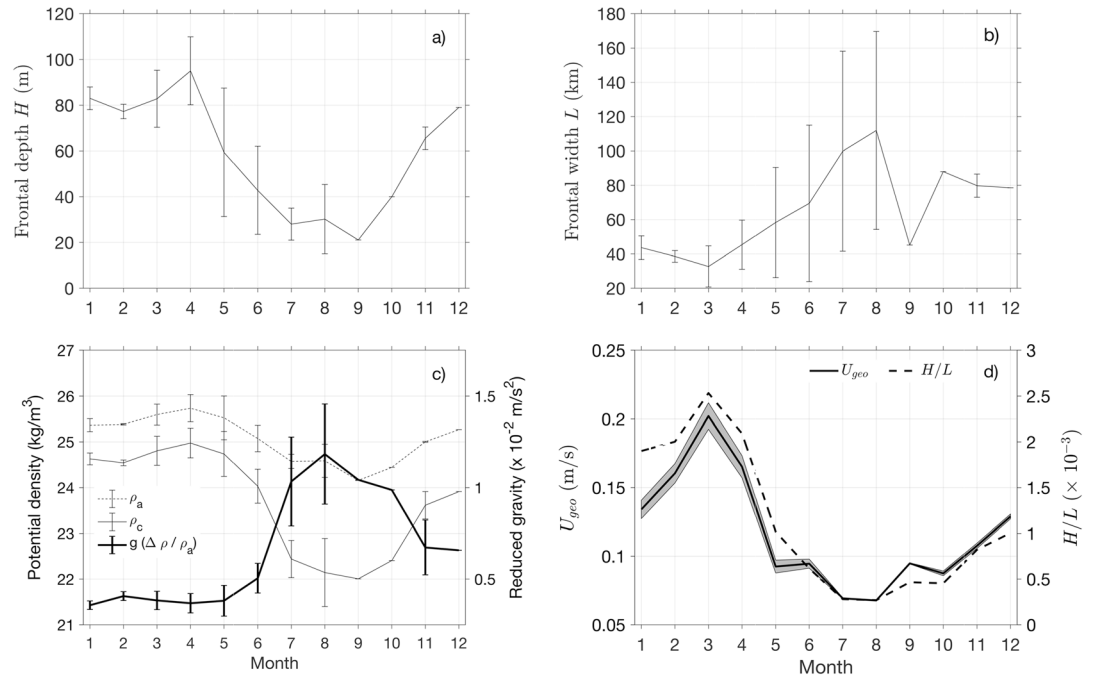


**Figure 5.** Monthly averaged frontal characteristics extracted from density transects along the Halifax Line using the algorithm described in section 3: (a) the frontal depth  $H$  (in meter), (b) the frontal width  $L$  (in kilometer), (c) the average potential density within the buoyant plume ( $\rho_c$ , in kilogram per cubic meter), the average potential density of ambient shelf water ( $\rho_a$ , in kilogram per cubic meter), and the value of the corresponding reduced gravity  $g'$  (in meter per square second). The error bars showed in these three panels correspond to one standard deviation of the observations. (d) Resulting  $U_{geo}$  (solid black line; in meter per second) along with the estimated error (shading; see Appendix A), and the ratio  $H/L$  (dashed black line).

in the wintertime, leading to the strong buoyancy-driven flow calculated in late winter. This result suggests that the variability in the steepness of the front ( $H/L$  in equation (2)) modulates the variability in  $U_{geo}$ , as opposed to the reduced density  $g'$ .

The impact of correcting for the wind-driven isopycnal tilting is examined by comparing  $U_{geo}$  to the corrected  $U_{geo}^c$  (Figure 6a). The magnitude of  $U_{geo}$  increases when corrected for wind-driven isopycnal tilting. This is due to the fact that monthly averaged alongshore winds are dominantly upwelling-favorable at the HL, therefore flattening isopycnals and leading to an underestimated  $U_{geo}$ . The maximum buoyancy-driven flow no longer occurs in the winter but during the fall. This new seasonal cycle coincides with the time of year when the reduced gravity is relatively high and the density front starts steepening. The phase shift in the seasonal cycle from winter to fall therefore suggests that correcting for the wind-driven isopycnal tilting seems to increase the role of the density gradient in modulating the alongshore buoyancy-driven flow.

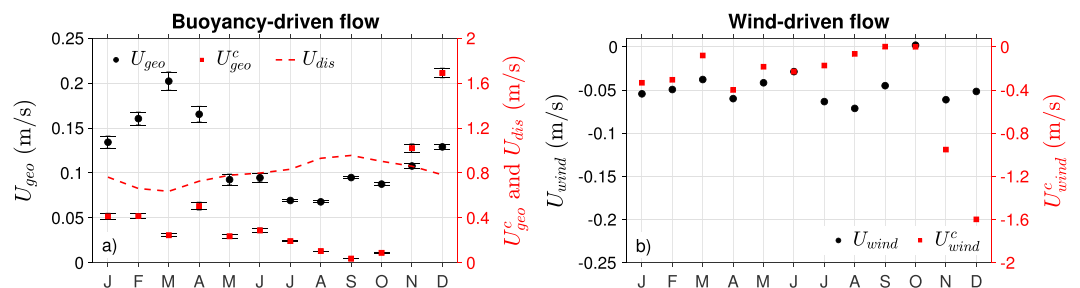


**Figure 6.** Monthly averaged noncorrected (black circles) and corrected (red squares) alongshore buoyancy-driven flow (a) and wind-driven flow (b) along the Halifax Line. Positive means southwestward. In panel (a), error bars indicate measurement errors on the computation of the buoyancy-driven flow (see Appendix A). The buoyancy-driven flow  $U_{dis}$  computed using WG05's approach is also superimposed (dashed line, see equation (5)).

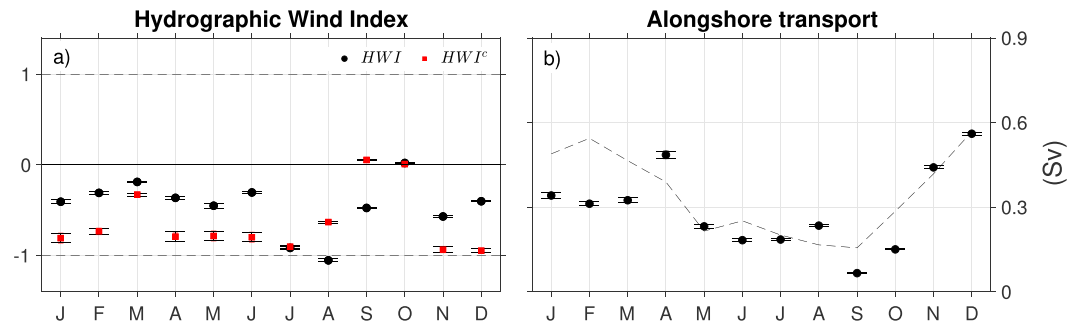


**Figure 7.** (a) Monthly averaged, noncorrected (black circles) and corrected (red squares) Hydrographic Wind Index (HWI) along the Halifax Line. (b) Monthly averaged alongshore transport  $Q = (U_{\text{geo}} + U_{\text{wind}})(HL/2)$  within the buoyant plume (in sverdrup, black circles) is shown along with the transport computed from the three acoustic Doppler current profilers (dashed line).

The corrected  $U_{\text{geo}}^c$  is, in theory, equivalent to the buoyancy-driven flow computed from the river discharge used in WG05 ( $U_{\text{dis}}$ ; using  $K = 4$  in equation (5)). However, a comparison between the two estimates yields significant differences between them (Figure 6a). Applying WG05's approach to the NSC fails to reproduce both the amplitude and the phase of the seasonal cycle of  $U_{\text{geo}}^c$ . Additionally, the buoyancy-driven flow derived from the upstream conditions ( $U_{\text{dis}}$ ) is overestimated for most of the year and peaks about 3 months earlier than  $U_{\text{geo}}^c$  (August–September versus November–December). This phase difference corresponds to the time lag associated with the downshelf propagation of the pulse of freshwater from Cabot Strait to the HL estimated in the literature (Dever, 2017; Drinkwater et al., 1979; Smith & Schwing, 1991). This discrepancy illustrates the advantages of using local conditions to determine the buoyancy-driven flow at a location far from the source of buoyant water.

#### 4.2. Isopycnal Tilting and Wind-Driven Flow

As shown in equation (11),  $U_{\text{wind}}$  is directly proportional to the alongshore wind speed. Analyzing the noncorrected  $U_{\text{wind}}$  therefore provides information on the alongshore wind speed. Figure 6b shows that the monthly averaged alongshore wind stress is mostly upwelling-favorable (i.e., negative or northeastward) at the HL. The monthly averaged alongshore wind stress exhibits two peaks of similar amplitude throughout the year. The fall and winter maximum is due to stronger winds, logically increasing the magnitude of the alongshore component. In summertime, winds tend to be weaker but are oriented in a more upwelling-favorable direction, also increasing the alongshore component.

Upwelling-favorable monthly winds tend to flatten the density front, leading to an underestimated  $U_{\text{geo}}$ . Correcting for the isopycnal tilting therefore increases the magnitude of  $U_{\text{geo}}$  (i.e., more positive) and consequently increases the magnitude of  $U_{\text{wind}}$  (i.e., more negative; Figure 6b). Although the monthly averaged wind direction provides information on the sign of the correction on  $U_{\text{geo}}$  (i.e., increase or decrease), no information on the amplitude of this correction can be deduced from the average wind direction and velocity. The amplitude of the correction for the wind-driven isopycnal tilting is contained in the variability of the wind stress at time scales close to the adjustment time scale (equation (8)); a larger, rapidly oscillating, wind stress will not drive the same isopycnal tilting as a constant, weaker, wind stress.

#### 4.3. HWI and Alongshore Transport

The difference between HWI and HWI<sup>c</sup> provides information on the impact of wind-driven isopycnal tilting on the alongshore current (Figure 7a). While the isopycnal tilting correction significantly affects the magnitude of  $U_{\text{geo}}$  and  $U_{\text{wind}}$  at the HL, it has a limited effect on the ratio of the two quantities, with the total alongshore flow dominated by the buoyancy-driven component most of the year.

Correcting for the wind-driven isopycnal tilting decreases HWI in every month except for August and September. The magnitude of the corrected HWI<sup>c</sup> has two yearly minima, indicating times when the buoyancy-driven flow modulates the NSC; the first local minimum is reached in winter, with  $HWI = -0.32$  in March, indicating that the buoyancy-driven flow is about 3 times as large as the wind-driven flow. The second local minimum is reached in the fall ( $HWI \approx 0$ ), showing that the buoyancy-driven flow almost entirely drives the NSC at that time of year. During the rest of the year, the wind-driven component plays a greater role in driving the NSC and at certain times almost balances the buoyancy-driven term, leading to  $HWI \approx -1$ .

The alongshore transport  $Q$  obtained by summing the buoyancy-driven and wind-driven flows ( $Q = (U_{\text{wind}} + U_{\text{geo}}) \times HL/2$ ) is compared to the alongshore transport computed from the velocity records collected at the three T-stations. These two estimates of the alongshore transport are not identical and cover slightly different areas: the former is estimated within the wedge-shaped current, whose dimensions vary with time, while the latter is computed between fixed locations (i.e., the T-stations). The two transport estimates nevertheless exhibit a similar seasonal cycle, where both the amplitude and phase are in good agreement ( $r = 0.78$ ,  $p < 0.01$ ). In both time series, the minimum transport is reached in the summer ( $\sim 0.20$  Sv), while the maximum occurs in winter ( $\sim 0.60$  Sv). The largest discrepancy between the two estimates occurs in the months of January, February, and March, where the alongshore transport computed between T1 and T3 is consistently larger than the transport deduced from the HWI approach. A possible explanation for this discrepancy is that the front outcrops around station T2 at this time of year (see Figures 4 and 6 in Dever et al., 2016). The alongshore transport-driven and buoyancy-driven terms is therefore logically smaller than the alongshore transport estimated from the ADCPs between T1 and T3. Nevertheless, the generally good agreement between the two estimates confirms the reliability of the HWI approach in capturing the alongshore transport variability to the first order of accuracy.

## 5. Discussion and Concluding Remarks

### 5.1. The HWI in the Context of WG05's Work

WG05's definition for the Wind Index constitutes a powerful tool to evaluate the downstream structure of a coastal current from a convenient, easily measurable, single variable (i.e., the river discharge). This approach, however, relies on assumptions that prevent the Wind Index from being generally applicable to buoyancy-driven coastal currents such as the NSC. First, it assumes that the only process taking place as the buoyant plume moves downstream is the *mixing between river water (with density  $\rho_r$ ) and ambient shelf water* (WG05). While that might be reasonable over short spatial scales ( $\mathcal{O}(10$  km)), adjustments need to be made to the Wind Index approach when considering scales on the order of  $\mathcal{O}(100$  km) in the alongshore direction, where many other processes affect the density field. The second assumption concerns the cross-shelf length scale associated with the density front, defined in WG05 as a constant linking the width of the current to the Rossby radius of deformation ( $K$  in equation (5)). As demonstrated in this study, the width of the current varies greatly with time. A time-dependent cross-shelf length scale ( $L$  in equation (3)) is therefore required when considering the NSC. Finally, by relying on upstream conditions ( $Q$ , and  $\rho_r$  in equation (5)), the time lag associated with the downshelf propagation of the signal coming from the source of buoyant water to the study region is not included. This lag can be significant (e.g., months) when investigating a buoyancy-driven coastal current over spatial scales on the order of  $\mathcal{O}(100$  km) such as the NSC (Dever, 2017; Dever et al., 2016). The method detailed in this study to estimate the HWI aims at addressing the assumption made in WG05 in order to extend the applicability of the Wind Index approach to the NSC. However, the HWI approach sacrifices the elegant simplicity of WG05's Wind Index approach and was only made possible by the availability of high-resolution data collected by underwater gliders. The relationship between data resolution and uncertainties in the HWI approach is addressed in the following section.

### 5.2. Data Resolution and Uncertainties in the HWI

The largest source of uncertainty in the HWI lies in the estimation of the frontal characteristics to determine the alongshore buoyancy-driven flow  $U_{\text{geo}}$  (see Appendix A). The uncertainty associated with each parameter in equation (2) is directly linked to the spatial resolution of the data set, which can greatly vary between data sources.

The mean densities of the coastal and ambient waters (i.e.,  $\rho_c$  and  $\rho_a$ , respectively) are averaged over a relatively large region. Their relative uncertainties are therefore at least 2 orders of magnitude smaller than the ones associated with the frontal dimensions ( $H$  and  $L$ ). The error associated with the frontal depth ( $\sigma_H$ ) originates from the vertical resolution of the observations, as well as from the horizontal sampling resolution that allows us to determine the location where the front intersects the bottom. We estimate the latter to be dominant and therefore scale  $\sigma_H$  with the error associated with the frontal width ( $\sigma_L$ ), using  $\sigma_H = \alpha \sigma_L$ . The relative error associated with the alongshore buoyancy-driven flow can thus be estimated using (see equation (A1)):

$$\frac{\sigma_{U_{\text{geo}}}}{U_{\text{geo}}} = \frac{\sigma_L \sqrt{\alpha^2 L^2 + H^2}}{HL}, \quad (20)$$

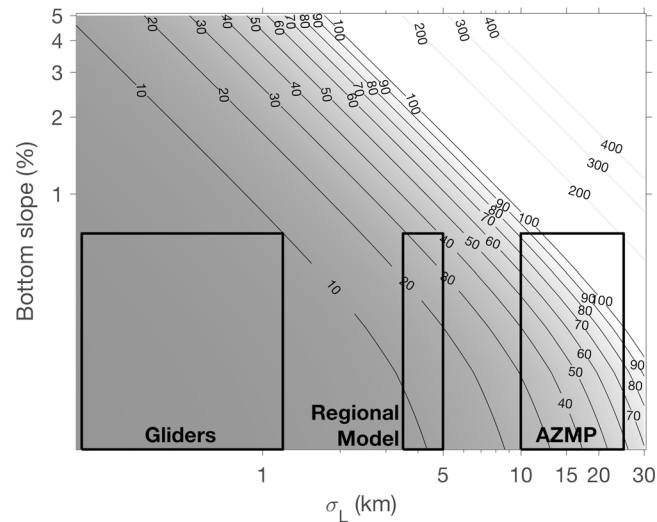


**Figure 8.** Relative error in  $U_{\text{geo}}$  (in percent) as a function of the horizontal uncertainty on the location of the front  $\sigma_L$  and the bottom slope (in percent), determined using the mode of the frontal dimensions measured by the glider in equation (20) ( $H = 87$  m,  $L = 50$  km). Thick black boxes indicate the range of the error in  $U_{\text{geo}}$  associated with glider data, a regional model with a grid resolution of  $1/16^\circ$  (Shan et al., 2016), and the Atlantic Zone Monitoring Program (AZMP). In each case, the horizontal uncertainty  $\sigma_L$  has been set to half the horizontal resolution.

where  $\sigma$  values denote the uncertainties. Figure 8 shows an example of the relative error in  $U_{\text{geo}}$  (in percent) as a function of the bottom slope  $\alpha$  and the uncertainty on the frontal width  $L$ , determined using the mode of the frontal dimensions at the HL, as measured by the glider ( $H = 87$  m,  $L = 50$  km; see section 3.5). It demonstrates that the relative error on the alongshore buoyancy-driven flow grows as the horizontal resolution of the data set becomes coarser or as the bottom slope steepens. Over the Scotian Shelf, using glider data guarantees a fairly low relative error ( $<10\%$ ) due to the high sampling resolution and the relatively gentle slope. Regional models with a relatively high resolution, such as the one introduced in section 2.4 (Shan et al., 2016, resolution of  $1/16^\circ$ ) can also be used to obtain a reasonable estimate of the alongshore buoyancy-driven flow. Ship-based monitoring programs such as the Atlantic Zone Monitoring Program (Therriault et al., 1998) have a coarser horizontal resolution, generating uncertainties in the estimation of the buoyancy-driven flow than can exceed the order of magnitude of the flow itself (Figure 8). This can be problematic when considering continental shelves with steeper bottom slopes ( $>4\%$ ; e.g., Oregon Shelf and Norwegian Shelf), where a high horizontal resolution is required. This highlights the need for higher-resolution data sets and the potential of underwater gliders to study coastal dynamics.

A secondary source of uncertainty arises from the time dependency of glider sampling. This is expected to introduced a degree of uncertainty in the HWI approach when the time it takes for the glider to capture the entirety of the density front (i.e., the observational time scale) is longer than the adjustment time scale. In this case, the front could have responded to a change in the alongshore winds before it was entirely sampled. This is, however, not expected to constitute a major source of uncertainty for two reasons: first, the observational time scale only exceeds the adjustment time scale in the summer months, when the frontal width ( $L$ ) is at its largest. Second, the fact that estimates of the buoyancy-driven and wind-driven flow are averaged monthly over several years is expected to reduce the impact of the uncertainty.

### 5.3. Concluding Remarks

The availability of independent ADCP current measurements across the NSC provided the opportunity to test the assumptions on which the HWI relies. The high correlation between the HWI-based and the ADCP-based alongshore currents ( $r = 0.90$ ) substantiates the two major assumptions associated with the HWI: (1) Most of the NSC's low-frequency variability can be captured by considering the alongshore buoyancy-driven and wind-driven circulation only and (2) the frictionally adjusted approximation holds for the NSC. This latter result concurs with Sandstrom (1980) that concluded that the frictionally adjusted theory could be applied to water depths up to 100 m over the inner Scotian Shelf, as long as the frictional adjustment time scale was chosen appropriately.

The HWI relies on the knowledge of the local cross-shelf density field and is therefore spatially dependent. The HWI is thus applicable to relatively large systems, such as the NSC, where downstream advective lags must be considered (Dever et al., 2016; Drinkwater et al., 1979). Previous studies relying on the transport and density of the upstream buoyant outflow to estimate the buoyancy-driven flow at a specific location (e.g., Münchow & Garvine, 1993a; WG05) neglected this advective lag, therefore limiting the spatial scales over which the analysis could be applied. Second, this spatial dependency allows the HWI to also be applicable to multisource buoyancy-driven currents, where the use of upstream conditions is difficult to justify given the presence of several sources of buoyant water with potentially overlapping plumes. Third, the HWI highlights the importance of the interaction between the density front associated with the buoyancy-driven coastal current and the alongshore surface winds. Our conclusions on the potentially large impact of local winds on the alongshore circulation agrees with Li et al. (2014) that attributes between 10% and 30% of the NSC low-frequency variability to changes in along-shelf winds, with important consequences on the distribution of freshwater as far as the Gulf of Maine. Our analysis of the wind-driven isopycnal tilting using a simple conceptual model also demonstrated that the large impact alongshore winds can have on the vertical density structure.

The HWI aims at scaling the respective contributions of wind and buoyancy to the total alongshore flow observed over the Scotian Shelf. Such a linear decomposition of the flow is useful to separate the dynamical mechanisms affecting coastal circulation, especially in a context of a changing climate where freshwater discharges and wind patterns are expected to evolve (Core Writing Team et al., 2007). Improving our understanding of the mechanisms driving the variability in shelf dynamics is relevant to many contemporary oceanographic challenges. In fact, a better understanding of shelf dynamics is key to address both biophysical (e.g., larvae dispersion or migratory routes; Dever, 2017; Vikebø et al., 2005) and geophysical (e.g., dispersion of sediment and pollutants) scientific questions. While this conceptual model can provide a good first-order approximation of the wind-driven cross-shelf circulation, truly separating the impact of surface winds from freshwater input remains a difficult challenge. The HWI conceptual model fails to describe other wind-driven circulation patterns such as coastal detachments (Fong & Geyer, 2001), baroclinic instabilities (Brink, 2016b), and relaxation of the density front in the absence of winds.

Based on this study, we conclude that the HWI approach presents key advantages toward a better understanding of the physical mechanisms forcing a buoyancy-driven coastal current. However, the HWI analysis is data intensive, since the measurement error on the buoyancy-driven current grows rapidly as the spatial resolution of the density field decreases. This only confirms the need for high-resolution transects of buoyancy-driven coastal currents in order to properly study the mechanisms at play. Conducting such surveys in various locations along the NSC's path could provide valuable insights into the spatial variability associated with the main driving mechanisms. Furthermore, comparative studies between different coastal currents (e.g., single source versus multisource) could be conducted using the HWI, for a better understanding of the dynamical differences characterizing these coastal systems.

### Appendix A: Errors on $U_{dis}$ and $U_{wind}$

The error associated with the estimated buoyancy-driven flow ( $U_{geo}$ ), wind-driven flow ( $U_{wind}$ ), and their respective transports are calculated based on the assumption that the variables are independent. It uses the following general equation for a function  $F = F(X, Y, \dots)$ :

$$\sigma_F = \sqrt{\left(\frac{\partial F}{\partial X} \cdot \sigma_X\right)^2 + \left(\frac{\partial F}{\partial Y} \cdot \sigma_Y\right)^2 + \dots} \quad (A1)$$

The error associated with  $U_{geo}$  (see equation (2)) can thus be expressed as follows:

$$\sigma_{U_{geo}} = |U_{geo}| \times \sqrt{\left(\frac{\rho_c}{\rho_a - \rho_c}\right)^2 \left[\left(\frac{\sigma_{\rho_a}}{\rho_a}\right)^2 + \left(\frac{\sigma_{\rho_c}}{\rho_c}\right)^2\right] + \left(\frac{\sigma_H}{H}\right)^2 + \left(\frac{\sigma_L}{L}\right)^2}. \quad (A2)$$

The error associated with  $U_{wind}$  (see equation (11)) is expressed as follows:

$$\sigma_{U_{wind}} = |U_{wind}| \times \sqrt{\frac{1}{2^2} \left[\left(\frac{\sigma_{\rho_{air}}}{\rho_{air}}\right)^2 + \left(\frac{\sigma_{\rho}}{\rho}\right)^2 + \left(\frac{\sigma_{C_{10}}}{C_{10}}\right)^2 + \left(\frac{\sigma_{C_D}}{C_D}\right)^2\right] + \left(\frac{\sigma_{U_{10}}}{U_{10}}\right)^2} \quad (A3)$$



The error associated with the transport (see equation (3)) can therefore be expressed as follows:

$$\sigma_Q = |Q| \times \sqrt{\left(\frac{\sigma_H}{H}\right)^2 + \left(\frac{\sigma_L}{L}\right)^2 + \left(\frac{\sigma_U}{U}\right)^2}. \quad (\text{A4})$$

The error associated with the HWI (see equation (19)) is expressed as follows:

$$\sigma_{HWI} = |HWI| \times \sqrt{\left(\frac{\sigma_{U_{wind}}}{U_{wind}}\right)^2 + \left(\frac{\sigma_{U_{geo}}}{U_{geo}}\right)^2} \quad (\text{A5})$$

### Acknowledgments

The authors would like to thank Richard Davis, Adam Comeau, and Jon Pye for making the required data sets available, as well as Sebastian Essink for his helpful reviews. This research was supported by the Ocean Tracking Network (OTN), through a network project grant (NETGP 375118-08) from the Natural Sciences and Engineering Research Council of Canada (NSERC) with additional support from the Canadian Foundation for Innovation (CFI, Project 13011), and the Social Sciences and Humanities Research Council (SSHRC 871-2009-0001). Additional funds were provided by the University in Bergen through the POME exchange program. The glider data used for this study are available at <http://gliders.oceantrack.org/>. ECMWF ERA\_Interim data product can be downloaded at <http://apps.ecmwf.int/datasets/>. The routines developed to compute the Hydrographic Wind Index can be found at [https://github.com/matdever/Ocean\\_Tracking\\_Network](https://github.com/matdever/Ocean_Tracking_Network).

### References

- Brink, K. H. (2016a). Continental shelf baroclinic instability. Part I: Relaxation from upwelling or downwelling. *Journal of Physical Oceanography*, *46*, 551–568. <https://doi.org/10.1175/JPO-D-15-0047.1>
- Brink, K. H. (2016b). Cross-shelf exchange. *Annual Review of Marine Science*, *8*, 59–78. <https://doi.org/10.1146/annurev-marine-010814-015717>
- Chapman, D. C., & Lentz, S. J. (1994). Trapping of a coastal density front by the bottom boundary layer. *Journal of Physical Oceanography*, *24*(7), 1464–1479. [https://doi.org/10.1175/1520-0485\(1994\)024<1464:TOACDF>2.0.CO;2](https://doi.org/10.1175/1520-0485(1994)024<1464:TOACDF>2.0.CO;2)
- Core Writing Team, Pachauri, R. K., & Reisinger, A. (2007). Climate change 2007: Synthesis report. Contribution of working groups I, II and III to the fourth assessment report of the intergovernmental panel on Climate change. Geneva, Switzerland: IPCC.
- Csanady, G. T. (1974). Barotropic currents over the continental Shelf. *Journal of Physical Oceanography*, *4*(3), 357–371. [https://doi.org/10.1175/1520-0485\(1974\)004<0357:BCOTCS>2.0.CO;2](https://doi.org/10.1175/1520-0485(1974)004<0357:BCOTCS>2.0.CO;2)
- Csanady, G. T. (1982). *Circulation in the Coastal Ocean*. Springer. <https://doi.org/10.1007/978-94-017-1041-1>
- Dee, D. P., Uppala, S. M., Simmons, A. J., Berrisford, P., Poli, P., Kobayashi, S., & Andrae, U. (2011). The ERA-Interim reanalysis: Configuration and performance of the data assimilation system. *Quarterly Journal of the Royal Meteorological Society*, *137*, 553–597. <https://doi.org/10.1002/qj.828>
- Dever, M. (2017). Dynamics of the Nova Scotia Current and its relationship with Atlantic salmon migration patterns over the Scotian Shelf (PhD thesis), Dalhousie University.
- Dever, M., Hebert, D., Greenan, B. J. W., Sheng, J., & Smith, P. C. (2016). Hydrography and coastal circulation along the Halifax Line and the connections with the Gulf of St. Lawrence. *Atmosphere-Ocean*, *54*, 199–217. <https://doi.org/10.1080/07055900.2016.1189397>
- Drinkwater, K., Petrie, B., & Sutcliffe, W. (1979). Seasonal geostrophic volume transports along the Scotian Shelf. *Estuarine and Coastal Marine Science*, *9*(1), 17–27. [https://doi.org/10.1016/0302-3524\(79\)90003-3](https://doi.org/10.1016/0302-3524(79)90003-3)
- El-Sabh, M. (1977). Oceanographic features, currents, and transport in Cabot Strait. *Journal of the Fisheries Research Board of Canada*, *34*(4), 516–528. <https://doi.org/10.1139/f77-083>
- Fong, D., Geyer, W., & Signell, R. (1997). The wind-forced response on a buoyant coastal current: Observations of the Western Gulf of Maine Plume. *Journal of Marine Systems*, *12*(1–4), 69–81. [https://doi.org/10.1016/S0924-7963\(96\)00089-9](https://doi.org/10.1016/S0924-7963(96)00089-9)
- Fong, D. A., & Geyer, W. R. (2001). Response of a river plume during an upwelling favorable wind event. *Journal of Geophysical Research*, *106*(C1), 1067–1084. <https://doi.org/10.1029/2000JC900134>
- Garvine, R. W. (1995). A dynamical system for classifying buoyant coastal discharges. *Continental Shelf Research*, *15*(13), 1585–1596. [https://doi.org/10.1016/0278-4343\(94\)00065-U](https://doi.org/10.1016/0278-4343(94)00065-U)
- Gill, A. (1982). *Atmosphere-ocean dynamics*. Elsevier Science.
- Lentz, S. J. (1995). U.S. contributions to the physical oceanography of continental Shelves in the early 1990's. *Reviews of Geophysics*, *33*(S2), 1225–1236. <https://doi.org/10.1029/95RG00177>
- Lentz, S. J., & Helfrich, K. R. (2002). Buoyant gravity currents along a sloping bottom in a rotating fluid. *Journal of Fluid Mechanics*, *464*, 251–278. <https://doi.org/10.1017/S0022112002008868>
- Li, Y., Ji, R., Fratantoni, P. S., Chen, C., Hare, J. A., Davis, C. S., & Beardsley, R. C. (2014). Wind-induced interannual variability of sea level slope, along-shelf flow, and surface salinity on the Northwest Atlantic shelf. *Journal of Geophysical Research: Oceans*, *119*, 2462–2479. <https://doi.org/10.1002/2013JC009385>
- Loder, J. W., Hannah, C. G., Petrie, B. D., & Gonzalez, E. A. (2003). Hydrographic and transport variability on the Halifax section. *Journal of Geophysical Research*, *108*, 8003. <https://doi.org/10.1029/2001JC001267>
- Münchow, A., & Garvine, R. W. (1993a). Buoyancy and wind forcing of a coastal current. *Journal of Marine Research*, *51*(2), 293–322. <https://doi.org/10.1357/0022240933223747>
- Münchow, A., & Garvine, R. W. (1993b). Dynamical properties of a Buoyancy-driven coastal current. *Journal of Geophysical Research*, *98*(C11), 20,063–20,077. <https://doi.org/10.1029/93JC02112>
- Ohashi, K., & Sheng, J. (2013). Influence of St. Lawrence River discharge on the circulation and hydrography in Canadian Atlantic waters. *Continental Shelf Research*, *58*, 32–49. <https://doi.org/10.1016/j.csr.2013.03.005>
- Pickart, R. S., McKee, T. K., Torres, D. J., & Harrington, S. A. (1999). Mean structure and interannual variability of the slope water system south of Newfoundland. *Journal of Physical Oceanography*, *29*(10), 2541–2558. [https://doi.org/10.1175/1520-0485\(1999\)029<2541:MSAIVO>2.0.CO;2](https://doi.org/10.1175/1520-0485(1999)029<2541:MSAIVO>2.0.CO;2)
- Sanders, T. M., & Garvine, R. W. (2001). Fresh water delivery to the continental shelf and subsequent mixing: An observational study. *Journal of Geophysical Research*, *106*(C11), 27,087–27,101. <https://doi.org/10.1029/2001JC000802>
- Sandstrom, H. (1980). On the wind-induced sea level changes on the Scotian shelf. *Journal of Geophysical Research*, *85*(C1), 461–468. <https://doi.org/10.1029/JC085iC01p00461>
- Schwing, F. B. (1989). Subtidal response of the Scotian shelf bottom pressure field to meteorological forcing. *Atmosphere-Ocean*, *27*(1), 157–180. <https://doi.org/10.1080/07055900.1989.9649332>
- Schwing, F. B. (1992a). Subtidal response of Scotian shelf circulation to local and remote forcing. Part II: Barotropic model. *Journal of Physical Oceanography*, *22*(5), 542–563. [https://doi.org/10.1175/1520-0485\(1992\)022<0542:SROSSC>2.0.CO;2](https://doi.org/10.1175/1520-0485(1992)022<0542:SROSSC>2.0.CO;2)
- Schwing, F. B. (1992b). Subtidal response of Scotian Shelf circulation to local and remote forcing. Part I: Observations. *Journal of Physical Oceanography*, *22*(5), 523–541. [https://doi.org/10.1175/1520-0485\(1992\)022<0523:SROSSC>2.0.CO;2](https://doi.org/10.1175/1520-0485(1992)022<0523:SROSSC>2.0.CO;2)

- Shan, S., Sheng, J., Ohashi, K., & Dever, M. (2016). Assessing the performance of a multi-nested ocean circulation model using satellite remote sensing and in situ observations. *Satellite Oceanography and Meteorology*, 1(1). <https://doi.org/10.18063/SOM.2016.01.004>
- Smith, P. C., & Schwing, F. B. (1991). Mean circulation and variability on the eastern Canadian continental shelf. *Continental Shelf Research*, 11, 977–1012. [https://doi.org/10.1016/0278-4343\(91\)90088-N](https://doi.org/10.1016/0278-4343(91)90088-N)
- Therriault, J., Petrie, B., Pepin, P., Gagnon, J., Gregory, D., Helbig, J., & Lefaiivre, D. (1998). Proposal for a Northwest Atlantic zonal monitoring program: Canadian technical report of hydrography and ocean sciences, 194. Retrieved from [www.dfo-mpo.gc.ca/Library/224076.pdf](http://www.dfo-mpo.gc.ca/Library/224076.pdf)
- Urrego-Blanco, J., & Sheng, J. (2014). Study on subtidal circulation and variability in the Gulf of St. Lawrence, Scotian Shelf, and Gulf of Maine using a nested-grid shelf circulation model. *Dynamics*, 64, 385–412. <https://doi.org/10.1007/s10236-013-0688-z>
- Vikebø, F., Sundby, S., Ådlandsvik, B., & Fiksen, O. (2005). The combined effect of transport and temperature on distribution and growth of larvae and pelagic juveniles of Arcto-Norwegian cod. *ICES Journal of Marine Science*, 62, 1375–1386. <https://doi.org/10.1016/j.icesjms.2005.05.017>
- Whitney, M. M., & Garvine, R. W. (2005). Wind influence on a coastal buoyant outflow. *Journal of Geophysical Research*, 110, 1–15. <https://doi.org/10.1029/2003JC002261>